

Spatial Fluctuations of the Intergalactic Temperature-Density Relation After Hydrogen Reionization

Laura C. Keating^{1,2,3*}, Ewald Puchwein^{1,2} and Martin G. Haehnelt^{1,2}

¹*Institute of Astronomy, University of Cambridge, Madingley Road, Cambridge, CB3 0HA, UK*

²*Kavli Institute for Cosmology, University of Cambridge, Madingley Road, Cambridge, CB3 0HA, UK*

³*Canadian Institute for Theoretical Astrophysics, 60 St. George Street, University of Toronto, ON M5S 3H8, Canada*

6 April 2024

ABSTRACT

The thermal state of the post-reionization IGM is sensitive to the timing of reionization and the nature of the ionizing sources. We have modelled here the thermal state of the IGM in cosmological radiative transfer simulations of a realistic, extended, spatially inhomogeneous hydrogen reionization process, carefully calibrated with Ly α forest data. We compare these with cosmological simulations run using a spatially homogeneous ionizing background. The simulations with a realistic growth of ionized regions and a realistic spread in reionization redshifts show, as expected, significant spatial fluctuations in the temperature-density relation (TDR) of the post-reionization IGM. The most recently ionized regions are hottest and exhibit a flatter TDR. In simulations consistent with the average TDR inferred from Ly α forest data, these spatial fluctuations have a moderate but noticeable effect on the statistical properties of the Ly α opacity of the IGM at $z \sim 4 - 6$. This should be taken into account in accurate measurements of the thermal properties of the IGM and the free-streaming of dark matter from Ly α forest data in this redshift range. The spatial variations of the TDR predicted by our simulations are, however, smaller by about a factor two than would be necessary to explain the observed large spatial opacity fluctuations on large ($\geq 50 h^{-1}$ comoving Mpc) scales at $z \gtrsim 5.5$.

Key words: galaxies: high-redshift – quasars: absorption lines – intergalactic medium – methods: numerical – dark ages, reionization, first stars

1 INTRODUCTION

Reionization is expected to be an extended, inhomogeneous process (e.g., Madau et al. 1999; Miralda-Escudé et al. 2000; Gnedin 2000; Furlanetto et al. 2004). This appears to be reflected in the observed rapid increase of opacity fluctuations of the IGM as probed by the Lyman- α (Ly α) forest at $z > 5$ (e.g., Becker et al. 2001; White et al. 2003; Songaila 2004; Fan et al. 2006). More recently, Becker et al. (2015) used new measurements of the effective optical depth of the Ly α forest in the spectra of quasars out to $z \sim 6$ to point out that the opacity fluctuations extend to rather large scales ($\geq 50 h^{-1}$ comoving Mpc) and are larger than can be explained with the evolution of the density field alone.

Using full radiative transfer simulations of the inhomogeneous reionization process, driven by massive stars in

high-redshift galaxies and calibrated with Ly α forest data, Chardin et al. (2015, 2017) argued that these fluctuations of the Ly α opacity on large scales may suggest a contribution to the UV background from rare, bright sources. Alternatively, Davies & Furlanetto (2016) have suggested that large fluctuations in the mean free path may source spatial fluctuations on large scales in a UV background from faint stellar sources, strongly amplifying fluctuations in the density field. Most relevant for the work presented here, D’Aloisio et al. (2015) considered the effect of spatial fluctuations of the temperature-density relation (TDR) in the post-reionization Universe caused by regions ionized at different redshifts. D’Aloisio et al. (2015) suggested that these are responsible for the large Ly α opacity fluctuations on large scales due to the temperature dependence of recombination rates. Note that the three different models make rather different predictions for the correlation between the large scale fluctuations of the Ly α opacity and the space density and brightness of

* E-mail: lkeating@cita.utoronto.ca

ionizing sources which should – at least in principle – be observable (see [Davies et al. 2017](#) for some recent modelling of the correlation between Ly α forest opacity and galaxy surface density of Ly α emitters).

Modelling all these effects accurately is numerically very challenging. It requires cosmological radiative transfer simulations that can properly model the temperature evolution during the inhomogeneous reionization. These simulations must also have sufficient dynamic range to resolve the sinks of ionizing radiation and at the same time capture the mean free path of ionizing photons, which is rapidly increasing when the individual ionized regions percolate at the end of the reionization process.

If reionization first proceeds in an inside-out fashion (e.g., [Furlanetto & Oh 2005](#); [Choudhury et al. 2009](#)), then the underdense voids will be the last to reionize and should have high temperatures after overlap. However, adiabatic cooling means that the expanding voids are also the most efficient at cooling so these fluctuations may fade away quickly ([Miralda-Escudé & Rees 1994](#); [Upton Sanderbeck et al. 2016](#)). There will also be fewer recombinations in the underdense gas and the photoheating rate will therefore be lower. The effect of the hotter voids may already be unimportant for measurements of the temperature of the IGM at $z < 5$ using the Ly α forest ([Becker et al. 2011a](#)), which is most sensitive to densities close to the mean. The impact of spatial fluctuations of the TDR may, however, nevertheless be present in higher-redshift statistics of the Ly α forest, such as the aforementioned distribution of Ly α optical depths and the flux power spectrum. The latter is particularly important for placing constraints on the mass of warm dark matter particles ([Viel et al. 2005, 2013](#); [Iršič et al. 2017](#)).

The effects of temperature fluctuations on the post-hydrogen reionization IGM have previously been discussed in several other works, using both semi-numerical models (e.g., [Furlanetto & Oh 2009](#); [Lidz & Malloy 2014](#); [D’Aloisio et al. 2015](#)) and radiative transfer simulations (e.g., [Trac et al. 2008](#); [Cen et al. 2009](#)). We use here new full cosmological radiative transfer simulations to obtain improved estimates of the expected spatial fluctuation of the TDR at the end of reionization. Our emphasis will be on models that are consistent with the temperature of the IGM at mean density inferred from Ly α forest data. We will perform a detailed direct comparison of mock absorption spectra obtained from our simulations with available Ly α forest data. Accurately predicting the effect the temperature fluctuations have on Ly α forest data will eventually require careful modelling of the ionizing sources in a multi-frequency radiative transfer simulation (e.g., [Pawlik & Schaye 2011](#)). This is unfortunately still beyond the scope of this paper and we will instead employ mono-frequency radiative transfer simulations for a range of photon frequencies. These simulations will allow us to estimate how long these fluctuations persist past reionization and the length scales over which they occur. By performing mono-frequency radiative transfer simulations for a range of photon frequencies we can also explore the range of models consistent with the mean TDR inferred from Ly α forest data.

We will further compare our simulations to estimates of the effect of spatial variations of the TDR of the IGM in the post-reionization Universe based on the hybrid approach employed by [D’Aloisio et al. \(2015\)](#) which combines

the results of suites of optically thin simulations without radiative transfer performed for a range of (instantaneous) reionization redshifts. For this we will perform our own suite of optically thin simulations that are instantaneously reionized at a range of redshifts. These are then combined with a reionization history taken from one of our radiative transfer runs.

The paper is structured as follows: in Section 2, we discuss the cosmological hydrodynamic and radiative transfer simulations we use to model the reionization of hydrogen. In Section 3, we discuss the temperature of the IGM after reionization has ended. In Section 4, we compare our simulations to several Ly α forest probes of the high-redshift IGM and discuss the effect of the spatially varying TDR due to inhomogeneous reionization. Finally, in Section 5, we present our conclusions. We assume the cosmology $\Omega_m = 0.308$, $\Omega_\Lambda = 0.692$, $\Omega_b = 0.0482$, $h = 0.678$, $\sigma_8 = 0.829$ and $n_s = 0.961$, consistent with the [Planck Collaboration XIII \(2016\)](#) results.

2 MODELLING REIONIZATION WITH OPTICALLY THIN AND RADIATIVE TRANSFER SIMULATIONS

As discussed in the introduction, we will model the effect of inhomogeneous reionization on spatial fluctuations of the intergalactic TDR with a suite of mono-frequency cosmological radiative transfer simulations, as well as with a hybrid approach based on a suite of optically thin simulations with a range of reionization redshifts. The radiative transfer simulations are performed in post-processing. They use the density fields taken from snapshots of the hydrodynamic simulation which was run with a homogeneous UV background. We use the same rate coefficients in our hydrodynamic and radiative transfer simulations. The recombination rates and collisional ionization rates are taken from [Hui & Gnedin \(1997\)](#). The collisional excitation rates are from [Cen \(1992\)](#). The Bremsstrahlung cooling rates are from [Osterbrock & Ferland \(2006\)](#) and the Compton cooling rate is from [Peebles \(1971\)](#).

2.1 Optically Thin Hydrodynamical Simulations

The cosmological hydrodynamic simulation we present here were run with the TreePM-SPH code P-GADGET3 (last described in [Springel 2005](#)). Our fiducial simulation was run in a box with side length $20 \text{ Mpc } h^{-1}$, containing 512^3 gas elements. We use the same initial conditions as the $20 \text{ } h^{-1} \text{ cMpc}/512^3$ box presented in the Sherwood Simulation Suite ([Bolton et al. 2017](#)), rerun to produce a finer output of snapshots and with the rate coefficients specified above. The mass of the gas particles is $m_{\text{gas}} = 8 \times 10^5 \text{ } h^{-1} M_\odot$ and the mass of the dark matter particles is $m_{\text{dm}} = 4.2 \times 10^6 \text{ } h^{-1} M_\odot$. We used a gravitational softening length of $1.6 \text{ } h^{-1} \text{ ckpc}$. Our fiducial simulation uses a simplified, computationally efficient model for star formation, designed for studies of the Ly α forest, where gas particles with $\Delta > 1000$ (where Δ is the density in units of the mean cosmic baryon density) and a temperature $T < 10^5 \text{ K}$ are turned into collisionless star particles ([Viel et al. 2004](#)). We assume a hydrogen mass fraction $X = 0.76$ throughout. We use the [Haardt & Madau](#)

Name	E_γ (eV)	Box Size (cMpc h^{-1})	τ	z_{reion}	$z_{0.5}$	Δz	$(a, z_1, \alpha_1, z_2, \alpha_2)$
RT	18.4	20	0.078	6.09	8.99	7.72	(1.05, 7.5, 0.5, 6.0, 1.5)
RT hot	23.8	20	0.078	6.15	9.16	7.59	(1.1, 8.0, 0.5, 6.0, 1.5)
RT 40 Mpc h^{-1}	18.4	40	0.078	5.99	9.29	7.97	(0.9, 7.5, 0.5, 6.0, 1.5)
RT fast	18.4	20	0.063	5.80	7.59	5.48	(1.05, 9.0, 2.0, 6.5, -0.5, 6.0, 1.5)

Table 1. Summary of the radiative transfer simulations presented in this paper. The columns show the photon energy E_γ , the box size, the optical depth to reionization τ , the redshift of reionization z_{reion} (defined as the redshift where the volume-weighted mean H I neutral fraction falls below $f_{\text{H I}} = 0.001$), the redshift at which $f_{\text{H I}} = 0.5$ and the extent of reionization Δz (defined as the difference between the redshift where $f_{\text{H I}} = 0.9$ and $f_{\text{H I}} = 0.001$). The final column shows the parameters used to modify the emissivity of the [Haardt & Madau \(2012\)](#) model, using equation 1. Note that the RT fast run contains an additional power-law term, so the parameters shown here correspond to the terms $(a, z_1, \alpha_1, z_2, \alpha_2, z_3, \alpha_3)$. All of these simulations are run on a grid with 512^3 cells.

(2012) uniform UV background, which turns on at $z = 15$ and assume ionization equilibrium. This UV background has previously been shown to reproduce constraints on the temperature of the IGM at $z > 3$ ([Puchwein et al. 2015](#)) (assuming ionization equilibrium), however it will neglect any inhomogeneous effects. We compare the thermal history and Ly α forest statistics computed from this simulation to those computed in our radiative transfer simulations throughout this paper (our “Uniform UVB” model). We also use the density fields taken from this simulation as input for our radiative transfer simulations (described below). This is to introduce some Jeans smoothing into the density field that otherwise would not be present in a simulation run without a UV background.

2.2 Radiative Transfer in Post-Processing

To explore a range of inhomogeneous reionization histories, we post-process our hydrodynamical simulation with a radiative transfer code. While this means that we neglect the hydrodynamic response to photoheating (e.g., smoothing of the density field), it allows us to explore different reionization histories in a relatively computationally inexpensive way. We use the radiative transfer code presented and described in detail in [Bauer et al. \(2015\)](#). This code solves the radiative transfer equation on a uniform Cartesian grid, using the M1 closure relation for the Eddington tensor. We have made some modifications to the treatment of the temperature. This includes the addition of adiabatic cooling due to the expansion of the Universe and adiabatic heating (cooling) due to collapse (expansion). The temperature change due to adiabatic evolution of a gas parcel is proportional to the rate of change of density, $\frac{d\Delta}{dt}$ (e.g. [Hui & Gnedin 1997](#)). We approximate this term by calculating the difference in density in a cell between two subsequent snapshots of our density field. We then use this rate to calculate a heating/cooling rate due the adiabatic evolution. We have tested this method on simple models where the density is increasing/decreasing with redshift and confirmed that it produces the desired results. We find that, in our implementation and at the densities probed by the Ly α forest, this term is almost always subdominant to the photo-heating, or to the combination of cooling due to Hubble expansion and Compton cooling.

Our fiducial simulation has a boxsize of 20 cMpc h^{-1} . To explore trends in the impact of temperature fluctuations with increasing volume, we also explore one run in a 40 cMpc h^{-1} box. We recognise that these volumes are small in the context of modelling reionization (e.g. [Iliev et al. 2014](#)).

However, as we wish to compare our results to absorption line studies of the IGM, we also require simulations with relatively high resolution (e.g. [Bolton & Becker 2009](#)). As we will show later, even in these smaller volumes, our resolution is still not high enough to properly model the Ly α forest on the smallest scales (see Section 4.2). Our smaller volumes also allow us to run many different reionization histories down to redshift 4, calibrating our emissivities until we found good agreement with properties of the post-reionization IGM. The disadvantage of these small volumes is that we do not model temperature fluctuations due to reionization on scales larger than the size of our box, which may be important for modelling the distribution of effective optical depths of the Ly α forest at these redshifts. Previous work in this area has focused on semi-numerical methods for modelling inhomogeneous reionization in large volumes ([D’Aloisio et al. 2015](#); [Davies et al. 2017](#)). The work presented here uses a very different method at higher resolution and should provide a useful contrast to what has been done before.

To calculate the emissivity in our simulation, we follow the method presented by [Chardin et al. \(2015\)](#). We find that the emissivity required to reionize our volume is sensitive to both the resolution of the box (as shown in [Chardin et al. 2015](#)) and also to the temperature of the gas. We assume an emissivity $\dot{N}_{\text{ion}} = b(z)\dot{N}_{\text{ion, HM12}}$ with $b(z)$ given by

$$b(z) = \begin{cases} a & \text{if } z > z_1, \\ a \left(\frac{z}{z_1} \right)^{\alpha_1} & \text{if } z_2 < z \leq z_1, \\ a \left(\frac{z_2}{z_1} \right)^{\alpha_1} \left(\frac{z}{z_2} \right)^{\alpha_2} & \text{if } z \leq z_2, \end{cases} \quad (1)$$

where a, z_1, z_2, α_1 and α_2 are constants and $\dot{N}_{\text{ion, HM12}}$ is the emissivity from [Haardt & Madau \(2012\)](#) integrated over all frequencies. We also include one run where we further lower the emissivity above $z = 9$, by adding another power-law term. The evolution of the integrated emissivities we assume are shown in the top left panel of Figure 1. We assign emissivities to haloes proportional to their dark matter masses ([Iliev et al. 2006](#)) and include the contribution of all haloes with FoF dark matter mass $M_{\text{halo}} > 1.2 \times 10^8 M_\odot$. The halo mass function in our simulation is more complete than in [Chardin et al. \(2015\)](#) at this mass (i.e., the turnover in our halo mass function occurs at a lower halo mass than in [Chardin et al. \(2015\)](#)), so we have a larger number of faint sources. This is likely due to differences in the halo finders used, the different gravity solvers or a different definition of the minimum number of dark matter particles for which haloes are said to be resolved. We find that we require lower emissivities than [Chardin et al. \(2015\)](#) to reionize a volume

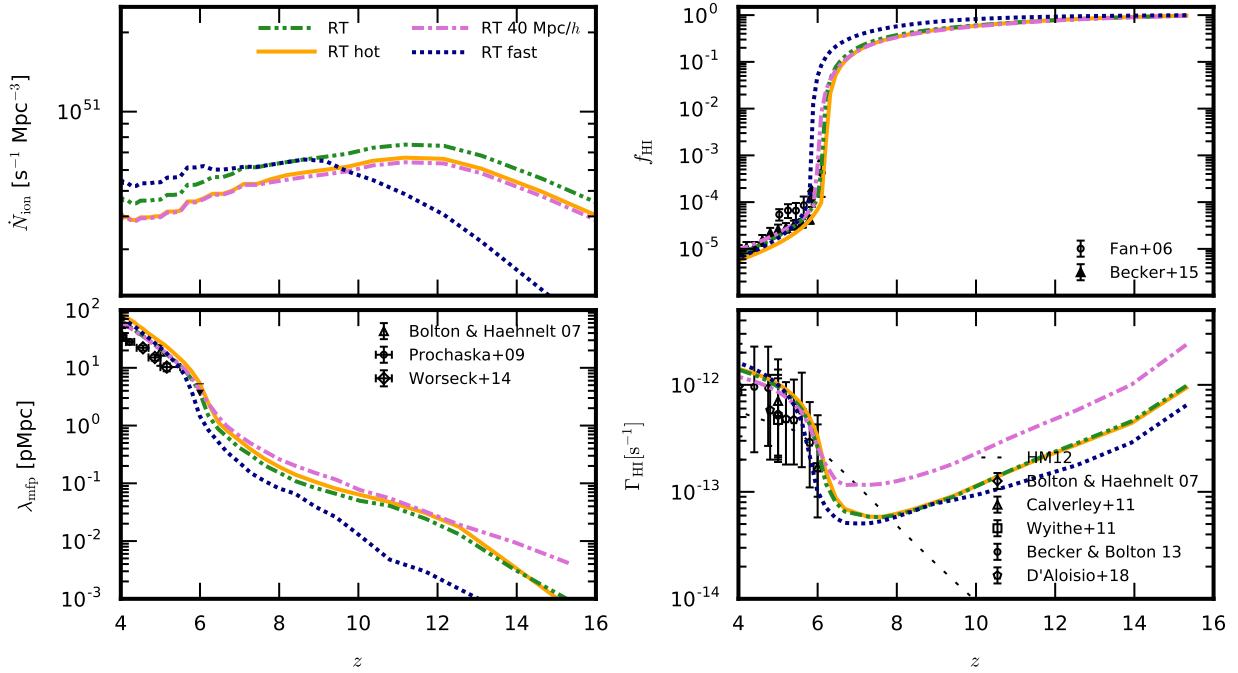


Figure 1. Top left: The emissivity we assume in our radiative transfer simulations as a function of redshift. Top right: The mean volume-weighted neutral hydrogen fraction we recover in our radiative transfer simulations. The black points are estimates of the H I fraction from the opacity of the Ly α forest taken from [Fan et al. \(2006\)](#) and [Becker et al. \(2015\)](#). Bottom left: The redshift evolution of the mean free path of a photon at 912 Å measured in our simulations. Also shown are results from [Bolton & Haehnelt \(2007b\)](#), [Prochaska et al. \(2009\)](#) and [Worseck et al. \(2014\)](#). Bottom right: The H I photoionization rate as a function of redshift in the radiative transfer simulations. Shown for comparison is the photoionization rate Γ_{HI} from [Haardt & Madau \(2012\)](#) (black dotted line) and estimates from observations (black points; [Bolton & Haehnelt 2007b](#); [Wyithe & Bolton 2011](#); [Calverley et al. 2011](#); [Becker & Bolton 2013](#); [D’Aloisio et al. 2018](#)).

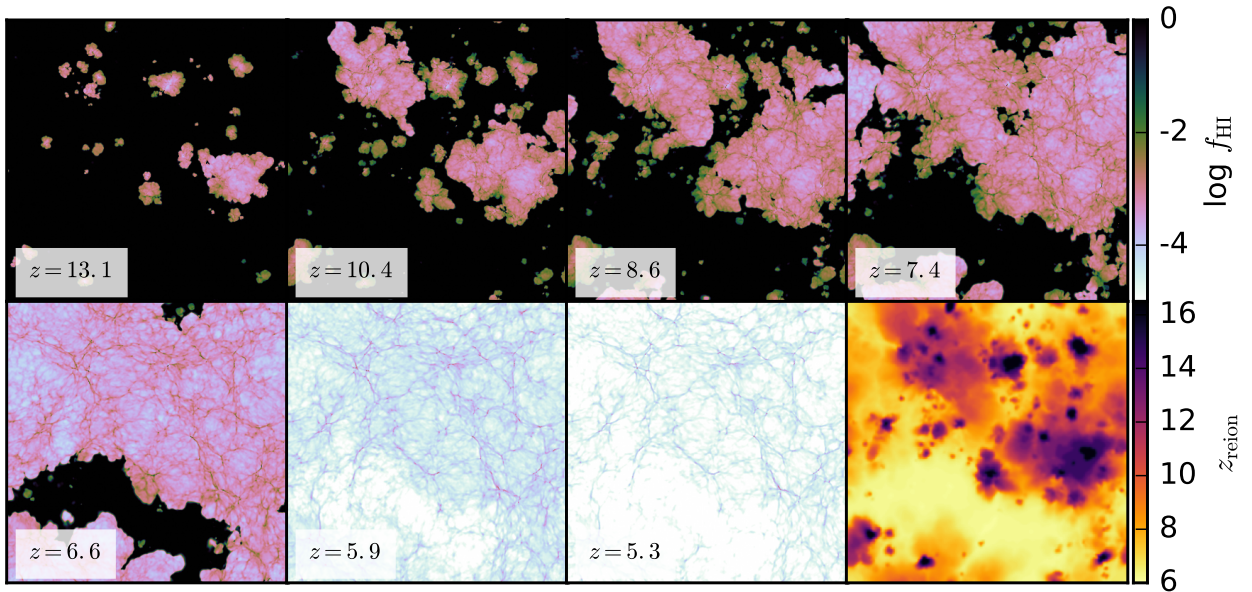


Figure 2. Redshift evolution of the hydrogen neutral fraction in a slice through the RT hot simulation. The thickness of the slice is $39.1 \text{ ckpc } h^{-1}$ and the width of the slice is $20 \text{ cMpc } h^{-1}$. Bottom right: The redshift at which each cell was first ionized (defined as the redshift when the neutral hydrogen fraction first dropped below one per cent).

of comparable resolution by the same redshift. This is likely because the gas in our box is generally hotter, resulting in a lower recombination rate. Our different star formation model will also be a contributing factor, as it removes all dense gas (rather than assuming some star formation efficiency) and this increases the “escape fraction” of our galaxies and reduces the clumping factor of the gas compared to the simulations of Chardin et al. (2015). It may also be due to the differences in the halo mass functions used to define the luminosity functions in the simulations, as discussed above.

We describe the different simulations we run in Table 1 and show our resulting reionization histories in the top right panel of Figure 1 and in Figure 2. As discussed in detail in Chardin et al. (2015) the evolution of the ionizing emissivity is tuned so that reionization ends at $z \sim 6$ in our radiative transfer runs, in agreement with estimates of the neutral fraction of the IGM using quasar absorption lines (Fan et al. 2006; Becker et al. 2015). In the bottom panels of Figure 1 we compare our simulation to two other probes of the ionization state of the IGM: the mean free path of a photon at 912 Å (bottom left panel) and the H I photoionization rate (bottom right panel). We measure the mean free path in the same way as Chardin et al. (2015). For our fiducial photon energy (discussed below), we find that our mean free path is about a factor of two higher than observations. The discrepancy is larger for the RT hot run which uses a higher photon energy. The photoionization rate we calculate is likewise too high by $z = 4$. This is unsurprising, since the photoionization rate scales proportionally with the mean free path. We have reasonable agreement for measurements of the photoionization rate at $z > 5$, however, where most of our analysis is focused.

As explained in the introduction, we run the radiative transfer simulations in mono-frequency mode for two different photon energies. To calculate a single photon energy from this spectrum, we take the frequency averaged excess energy of the ionizing photons. This is given by

$$E_\gamma - E_{\text{H I}} = \frac{\int_{\nu_{\text{H I}}}^{\infty} d\nu \frac{4\pi J_\nu}{h\nu} \sigma_{\text{H I}}(\nu) (h\nu - h\nu_{\text{H I}})}{\int_{\nu_{\text{H I}}}^{\infty} d\nu \frac{4\pi J_\nu}{h\nu} \sigma_{\text{H I}}(\nu)}, \quad (2)$$

where E_γ is the total photon energy, $E_{\text{H I}}$ is the ionization energy of H I, ν is the frequency, J_ν is the blackbody spectrum and $\sigma(\nu)$ is the cross section. Following Pawlik & Schaye (2011), we consider two cases for the photon energies. The first is the optically thick limit, which is calculated assuming $\sigma_{\text{H I}}(\nu) = 1$. There is no frequency dependence here as all ionizing photons are assumed to be absorbed. The second case is the optically thin limit where $\sigma_{\text{H I}}$ is the usual photoionization cross section for H I. We assume that all our sources emit with a $T = 70000$ K blackbody spectrum. This was chosen so that the radiative transfer runs with photon energies corresponding to the optically thin limit provided a good match for temperatures inferred from Ly α forest data (e.g., Becker et al. 2011a). Pawlik & Schaye (2011) found that the optically thin limit produced photoheating rates in better agreement with multi-frequency radiative transfer simulations in regions far from the sources when compared to the optically thick limit. For the optically thin limit, this corresponds to a photon energy $E_\gamma = 18.4$ eV. For the optically thick limit we get a photon energy $E_\gamma = 23.8$ eV. We

also calculate the average photoionization cross section corresponding to our spectrum, giving $\sigma_{\text{H I}} = 2.3 \times 10^{-18} \text{ cm}^2$.

For a given photon energy E_γ , the temperature change ΔT of the gas as it is ionized should be

$$E_\gamma - E_{\text{H I}} \approx \frac{3k_{\text{b}}}{2} \frac{\Delta T n_{\text{tot}}}{n_{\text{H}}} \quad (3)$$

Here, $E_{\text{H I}}$ is the ionization energy of hydrogen, k_{b} is the Boltzmann constant, n_{H} is the hydrogen number density and n_{tot} is the total number of particles. We take $n_{\text{tot}} = (2 + Y/4X)n_{\text{H}}$ which corresponds to ionized hydrogen and neutral helium, where $X = 0.76$ is the hydrogen mass fraction and $Y = 1 - X$ is the mass fraction of helium. Then, for the photon energy $E_\gamma = 23.8$ eV ($\Delta E = 10.2$ eV), this corresponds to $\Delta T \approx 38000$ K. For the photon energy $E_\gamma = 18.4$ eV ($\Delta E = 4.8$ eV), this corresponds to $\Delta T \approx 18000$ K. For a test simulation where we ionize the gas instantaneously and neglect any cooling, we indeed recover this temperature. This is shown in the left panel of Figure 3 for two different photon energies, representing the optically thin and thick cases for the spectrum we use throughout this work. The gas was reionized instantaneously by injecting photons into every cell. The majority of our gas has temperatures that agree well with the analytic prediction (dashed line). Gas towards higher densities has temperatures that lie above the line, likely due to additional photoheating following recombinations. In practice, however, an ionization front will move at a finite speed through the IGM and the gas will cool behind it. The peak temperatures achieved in the radiative transfer simulations are therefore usually less than the temperature changes quoted above.

2.3 Hybrid Model

In order to compare our radiative transfer simulations to the hybrid approach employed by D’Aloisio et al. (2015) we have run a suite of simulations that are reionized “by hand” at a range of redshifts. We construct this suite using eight outputs from a simulation run without a UV background. These snapshots are spaced 80 Myr apart, from $z = 12.2$ to 5.9. For each snapshot, we reinitialise the temperature and ionization state of each gas particle. We assume the temperature of recently ionized gas is 30000 K (as was assumed in D’Aloisio et al. 2015). If the temperature of the gas particle is less than this, we set the initial temperature of the gas to 30000 K. If the temperature of the particle is greater than this, we keep the temperature of the gas particle from the hydrodynamic simulation (to account for the hotter shock heated gas). The initial ionization state of the gas is computed assuming ionization equilibrium assuming a modified version of the Haardt & Madau (2012) UV background (described below). The simulations are then restarted from the altered snapshots and run down to $z = 4$.

We run these restarted simulations with a modified version of the Haardt & Madau (2012) UV background, which has an increased amplitude above $z = 6$ to ensure that the gas remains ionized (with the standard Haardt & Madau (2012) background the hydrogen recombines again). The middle panel of Figure 3 shows the effect of changing the UV background. We tested this using a code which solves for the temperature evolution with redshift of a gas element at mean density. If we use the standard Haardt & Madau

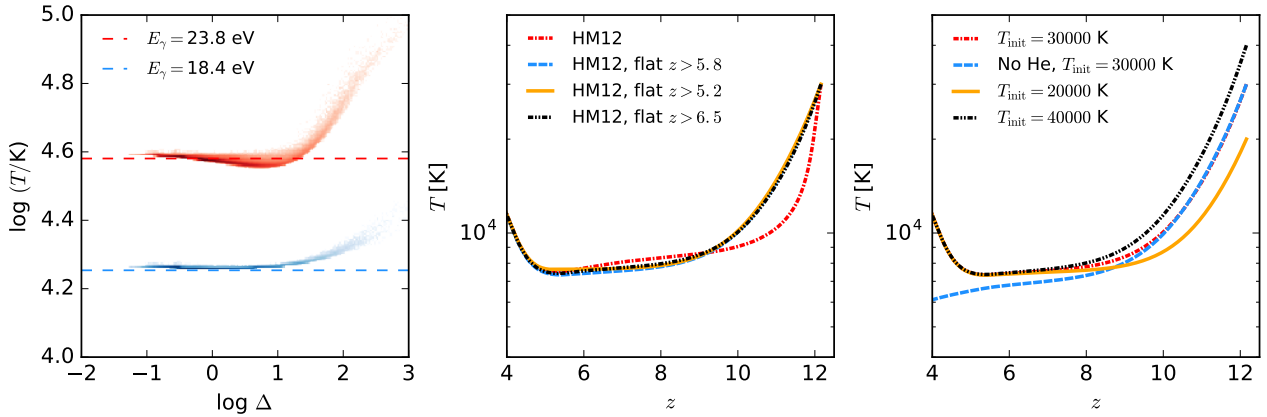


Figure 3. Left: Simple test of how hot the gas in the radiative transfer simulation becomes if cooling is neglected. The red and blue contours represent two different photon energies. The dashed lines are the expected temperature for this energy directly after the gas is ionized. However, due to the finite velocity of the ionization front, we do not generally see temperatures this high in the radiative transfer simulations. Middle: Temperature evolution of gas at mean density for different assumptions about the amplitude of the UV background, assuming the gas is initially ionized and has a temperature of 30000 K. This was calculated by solving for the thermal history of a gas parcel at mean cosmic baryon density, rather than in a full radiative transfer simulation. The evolution of the temperature with redshift does not depend on the choice of UV background, as long as the UV background is strong enough to keep the gas ionized. Right: Temperature evolution of gas at mean density, assuming different initial temperatures. Again, this was calculated by solving for the thermal history of a gas parcel at mean cosmic baryon density. Also shown is a run where heating/cooling due to helium is neglected.

(2012) background, we find that this is too low at high redshift to keep the gas ionized. The partially neutral gas can then cool rapidly via collisional ionization and excitation in addition to Compton cooling (which is what we see for using Haardt & Madau (2012), red dash-dotted line). As long as the gas remains ionized, the results are reasonably insensitive to the amplitude of the UV background (blue dashed and black dot-dot-dashed lines, which have photoionization rates a factor of two higher/lower than the fiducial case shown by the orange solid line). At lower redshift, we find that the model run with Haardt & Madau (2012) is slightly hotter, due to the gas being photoheated as it is reionized. We modify the photoheating rates in the same way as the photoionization rates.

We also investigate the impact of changing the temperature of the recently ionized gas (right panel of Figure 3). We increase/decrease our initial temperature by 10000 K. All the runs converge to the same temperature within about 300 Myr. We also look at the effect of neglecting helium in our thermal evolution (blue dashed line). The most noticeable difference is that the temperature begins to rise in our other models below $z \sim 5$, due to the onset of He II reionization.

We use our grid of instantaneous reionization simulations to construct the thermal history of the IGM. This is accomplished by first calculating the reionization redshift of each cell in the RT hot simulation (which reaches temperatures similar to our hybrid model). We define the reionization redshift as the redshift when the neutral hydrogen fraction of a cell first falls below one per cent. An example of the resulting distribution of redshifts is shown in the bottom right panel of Figure 2. We map the instantaneous reionization hydrodynamic simulations onto a 512^3 grid, the same resolution as our radiative transfer simulations. The hybrid model is also constructed on a 512^3 grid. For each cell of the hybrid model, we assign a temperature, density and neu-

tral fraction taken from the instantaneous simulation that ionized at a redshift closest to the reionization redshift of that cell. This leaves us with a model that has a spatially varying temperature-density relation similar to our radiative transfer models, but with coarser time resolution (due to the finite number of instantaneous reionization simulations we have run) and which takes the hydrodynamic response of the gas due to photoheating into account.

3 TEMPERATURE INHOMOGENEITIES AT THE END OF REIONIZATION

3.1 Temperature Evolution

To compare the results from our radiative transfer and optically thin simulations to those of D’Aloisio et al. (2015), we study the temperature evolution of regions of the IGM that reionized at the same redshift. In the radiative transfer simulation, we select cells that reionized at the same time and follow their thermal evolution. These redshifts are assigned by choosing the redshift of the snapshot where the neutral fraction of the cell first dropped below one per cent. This means that the time resolution of our redshifts is limited to the spacing of the snapshots, which are taken every 20 Myr. The resulting evolution of the volume-weighted mean temperature is shown in the left and middle panels of Figure 4 for radiative transfer simulations with two different photon energies. We show the temperature evolution of all the gas (top) and of gas with an density $\Delta < 0.3$ (bottom). We do not account for evolution of the density field when we select these cells. The gas associated with collapsing/expanding objects may end up in a different cell by $z \sim 4$. However, this should give an indication of the level of temperature fluctuations in the IGM that one may expect after reionization. We show here cells that reionized at redshifts in intervals of 80 Myr, to match the temporal resolution of our

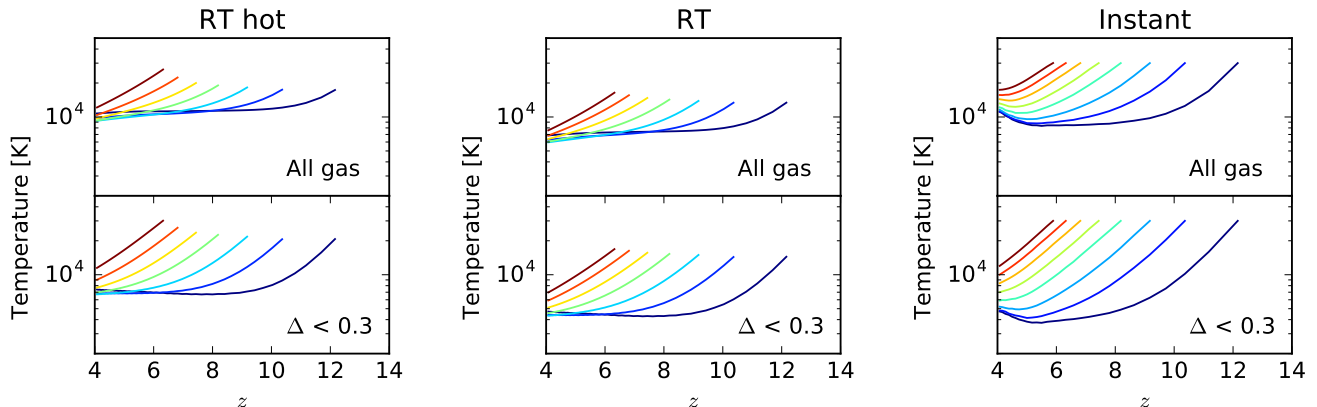


Figure 4. Left: Temperature evolution of cells in the radiative transfer simulation with $E_\gamma = 23.8$ eV that reionized at the same redshift for all gas (top) and gas with density $\Delta < 0.3$ (bottom). Middle: The same, but for a photon energy $E_\gamma = 18.4$ eV. Right: The same, but for the simulations that were reionized instantaneously.

hybrid model. Note that in our radiative transfer simulation cells reionize in between these intervals also. In the right panel we present the temperature evolution of the eight instantaneous reionization simulations. In this case we present results averaged over the entire box, rather than a subset of cells as before.

For the radiative transfer runs, we find that the initial temperature of our ionized cells is not constant with redshift. We also do not find temperatures as high as seen in our earlier photon energy tests (left panel of Figure 3). This is partly because the cells do not ionize instantaneously, so cooling will occur in tandem with the photoheating. It is also due to the difficulty in selecting the reionization redshift in post-processing: cells that reionize just after a snapshot is taken will have had time to cool before the next output. For most of the redshift bins, the gas temperature decreases monotonically with decreasing redshift. The exception is the gas with $\Delta < 0.3$ in the highest redshift bin (at $z \sim 12$). Here, the temperature does decrease initially but then begins to increase slightly below $z = 8$. This effect is likely due to how we are assigning reionization redshifts to each cell and that we are neglecting the advection of gas across cell boundaries. As expected, the low-density gas (bottom panel) cools to lower temperatures than the average of all gas due to the adiabatic expansion of the voids and the lower amount of photoheating in the low-density gas. This suggests that our simple implementation of adiabatic heating/cooling in post-processing is performing adequately. We find that the gas that reionized early (with a reionization redshift $z \sim 12$) does not cool as efficiently as the gas which ionized later. This can probably be explained by the different density distributions in the different reionization redshift bins. Gas that was ionized early on samples more biased regions of the IGM, and will have a density PDF that is skewed towards higher densities than the density PDF of the whole volume. The higher density will result in more recombinations and hence more heating by subsequent photoionizations. There may also be an additional contribution from adiabatic heating due to collapse, but we generally find that this effect is small compared to the photoheating rate.

Comparing the results of our simulations run with different photon energies, we find that the initial temperature of the gas is higher in the higher photon energy simulation as expected, but the difference is not as large as in the left panel of Figure 3. Again, this is likely due to the recently ionized gas cooling in between snapshots. The maximum temperature attained immediately after reionization is smaller at higher redshift, likely due to the increasing efficiency of Compton cooling. The gas is also able to cool to lower temperatures in the run with $E_\gamma = 18.4$ eV, as the photoheating rate due to recombinations is lower in this case.

For the optically thin hydrodynamic simulations, the results are qualitatively similar, with the gas cooling to a similar temperature to the RT run. One notable difference is the effect of including helium as already discussed in Section 2.3. Around $z \sim 5$ the temperature of the gas begins to increase again. This upturn is present in all of our models. Note that we will not model the patchiness of He II reionization. The overall effect is to reduce the temperature contrast between our models after hydrogen reionization has ended.

The results of our simulations are qualitatively similar to those presented in D’Aloisio et al. (2015) but suggest smaller spatial fluctuations of the TDR. Neither the radiative transfer or hydrodynamic runs contain gas as cold ($T \sim 3000$ K for $\Delta < 0.3$ at $z = 5$). In the optically thin simulations, the scatter in temperature at $z \sim 5.5$ is more like a factor of 3 rather than the factor of 5 that D’Aloisio et al. (2015) find. This will however be sensitive to when He II reionization is assumed to begin, but note that Becker et al. (2011a) finds that the temperature of the IGM is already beginning to increase below $z \sim 4.8$. For the radiative transfer simulations the scatter is further reduced.

In Figure 5 we show the evolution of the temperature at mean density (T_0) with redshift for our uniform UVB, radiative transfer and hybrid models. To calculate T_0 , we select cells with densities within 5 per cent of the mean and take the volume-weighted mean of their temperatures. Also shown for comparison are measurements of the IGM temperature from Becker et al. (2011a) and Bolton et al. (2012). The measurement from Bolton et al. (2012) is an estimate

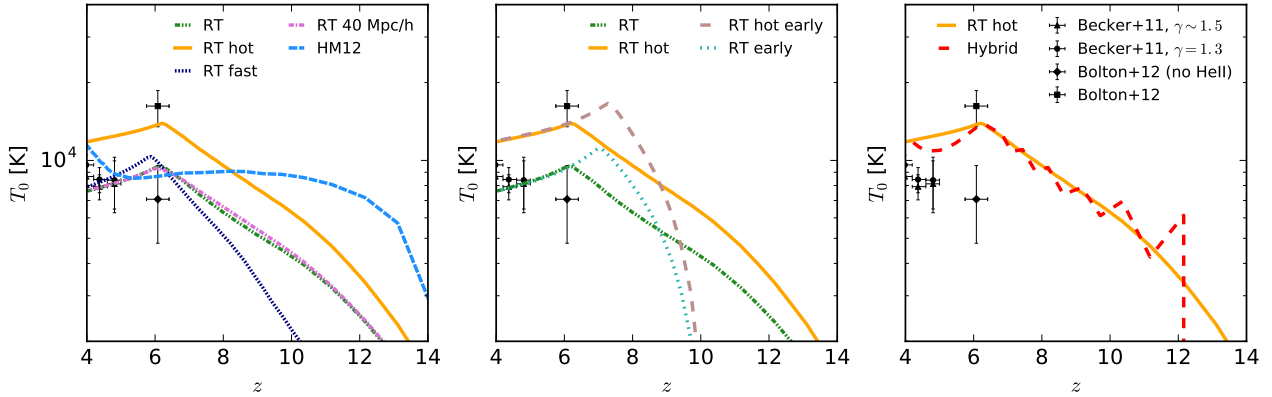


Figure 5. Evolution of the volume-weighted mean temperature at mean density with redshift for the different methods of modelling the temperature evolution, different photon energies and different reionization histories. Plotted for comparison are measurements of the IGM temperature from [Becker et al. \(2011a\)](#) for two different values of the slope of the temperature-density relation γ , which maps the temperature measured at the characteristic density probed by the Ly α forest to the temperature at mean density. We also show a measurement from [Bolton et al. \(2012\)](#) measured around a quasar near-zone and an estimate of the temperature where the likely contribution from He II heating due to the quasar is subtracted.

of the temperature around a quasar near-zone, so there is likely to be extra heating due to He II ionization close to the quasar (e.g., [Bolton & Haehnelt 2007a](#); [Keating et al. 2015](#)). The effect of this extra source of heating was modelled and subtracted to estimate the temperature of the IGM at $z = 6$. In Figure 5, we show the measured temperature with a contribution from He II heating and an estimate of the temperature where the likely contribution of He II heating has been subtracted. In the left panel we show results from the radiative transfer simulations presented in Table 1 and our uniform UVB model. The uniform UVB model predicts gas temperatures a few times 10^3 K already at $z = 14$, since the [Haardt & Madau \(2012\)](#) UV background turns on at $z \sim 15$. It reaches a peak at $z \sim 8$, then declines until the onset of He II reionization which begins around $z \sim 5$ when it rises again. The temperature in the radiative transfer runs rises more steeply. The gas at mean density is cooler than the uniform UVB run up until $z \sim 7$. It continues to rise until overlap occurs at $z \sim 6$ after which it cools due to Hubble expansion and Compton cooling. Increasing the energy of the photons increases the temperature of the gas somewhat. We find no trend with boxsize for the two simulations with the same photon energy. Changing the ionization history does change the temperature evolution of the gas as expected. We have also computed the curvature of our spectra at $z = 4.8$ to compare directly to the [Becker et al. \(2011a\)](#) measurements. The trend among the models is consistent with what we show here, although we do find a slightly larger difference between the models and the data (a difference of 0.1 dex in the curvature between the RT model and the [Becker et al. \(2011a\)](#) measurement at $z = 4.8$). This may be due to differences in the noise treatment.

In the middle panel we explore the temperature evolution of two other radiative transfer runs. We note that these runs have not been tuned to match Ly α forest constraints on IGM properties at lower redshifts (such as the photoionization rate) and we will therefore not discuss them elsewhere in this paper. Even so, it is still interesting to investigate their temperature evolution, which should not depend on the am-

plitude of the UV background. As shown in the left panel of Figure 5, we see that at $z \sim 5$, the temperature of our RT hot run is too high to be compatible with observations. We have checked if this could be remedied if reionization occurred earlier, giving the gas more time to cool before the beginning of He II reionization. We explore this by looking at runs for both photon energies we use here, where reionization is faster and finishes at $z \sim 7.5$. We find that for a faster reionization, the peak of the evolution of T_0 with redshift occurs at a higher temperature. This is because the reionization redshifts of different regions are closer together and the gas has not had time to cool significantly before reionization ends. The filling factor of hot gas will be higher and this is reflected in the average.

Once reionization has ended in all models, the gas begins to cool and models with constant E_γ follow a common evolution for T_0 with redshift which is set by the energy injected by photoheating due to recombinations and subsequent ionizations. Therefore, even for models where reionization occurs early, it is difficult to reconcile temperature boosts as high as assumed in [D’Aloisio et al. \(2015\)](#) with measurements of the IGM temperature at $z \sim 5$. This is in contrast to the results of [Upton Sanderbeck et al. \(2016\)](#), who find temperatures consistent with the [Becker et al. \(2011a\)](#) measurements assuming a linear reionization history and that gas is heated to 30000 K as it is ionized. This may be due to the different reionization history, or to the hardness of the spectrum assumed which affects how quickly the gas cools. Following hydrogen reionization the photoheating rates are expected to decrease due to a large increase in the mean-free path for ionizing photons and the resulting change from the optically thick to the optically thin regime ([Abel & Haehnelt 1999](#); [Puchwein et al. 2015, 2018](#)). A realistic temperature evolution may therefore fall closer to our hot model before hydrogen reionization and closer to our fiducial model after hydrogen reionization. Investigating this properly will require multi-frequency radiative transfer simulations with realistic source spectra.

In the right panel we compare our hybrid simulation

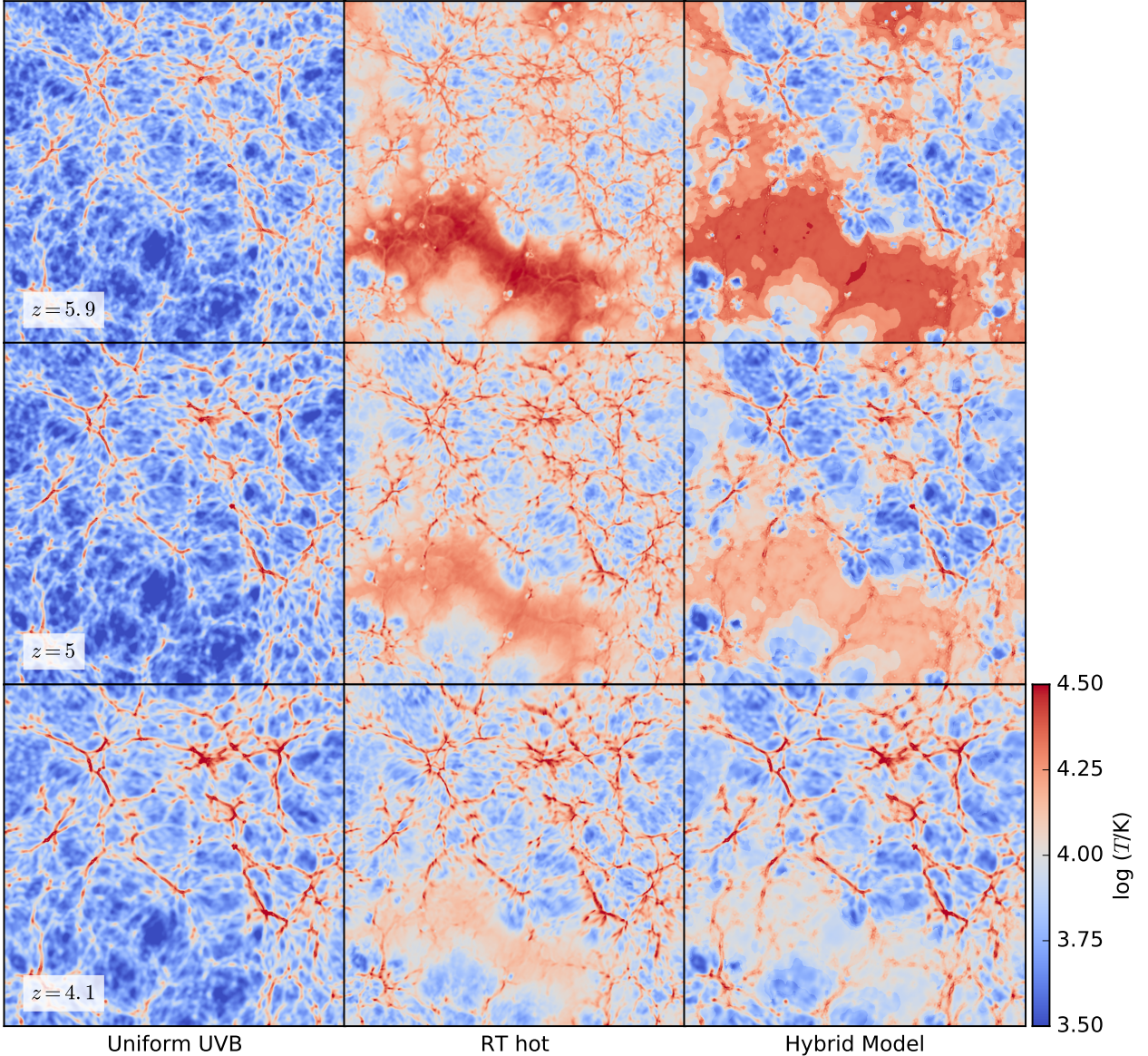


Figure 6. Temperature of the gas in the same slice shown in Figure 2 for the three models for three post-reionization redshifts. The hottest gas in the uniform UVB simulation lies in the adiabatically heated filaments and haloes. In the radiative transfer and hybrid models, spatial fluctuations in the temperature of the IGM due to reionization are present and the recently ionized low density gas is hot.

with the radiative transfer simulation which has the closest temperature. This is the RT hot run. The temperature evolution in the hybrid model is not entirely smooth, due to the finite number of instantaneous reionization simulations in our suite of optically thin simulations. The temperature does not increase monotonically but instead oscillates, with each peak corresponding to the redshift of one of the instantaneous simulations. Overall the evolution of T_0 is, however, in good agreement with that of the corresponding radiative transfer simulation. Again, we find that this model with the higher photon energy does not agree with the observational constraints on the temperature at lower redshift. This suggests that models where gas receives a temperature boost as large as $T = 30000$ K after reionization do not agree with the Ly α forest data.

3.2 Temperature Fluctuations

In Figure 6, we show the projections of the IGM temperatures predicted by our three models at three different redshifts. The radiative transfer simulation we show here is the RT hot run, which has a T_0 evolution most similar to the hybrid model. The optically thin case shows less fluctuations on large scales, as it was run with a spatially uniform UV background. The hottest gas is found in the collapsing haloes and filaments and the voids have all cooled efficiently as they expand. The radiative transfer and hybrid models both show increased temperatures ($T > 10^4$ K) in regions that reionized later (compare with the map of reionization redshifts in the bottom right panel of Figure 2). The regions that reionized later correspond to the low-density regions.

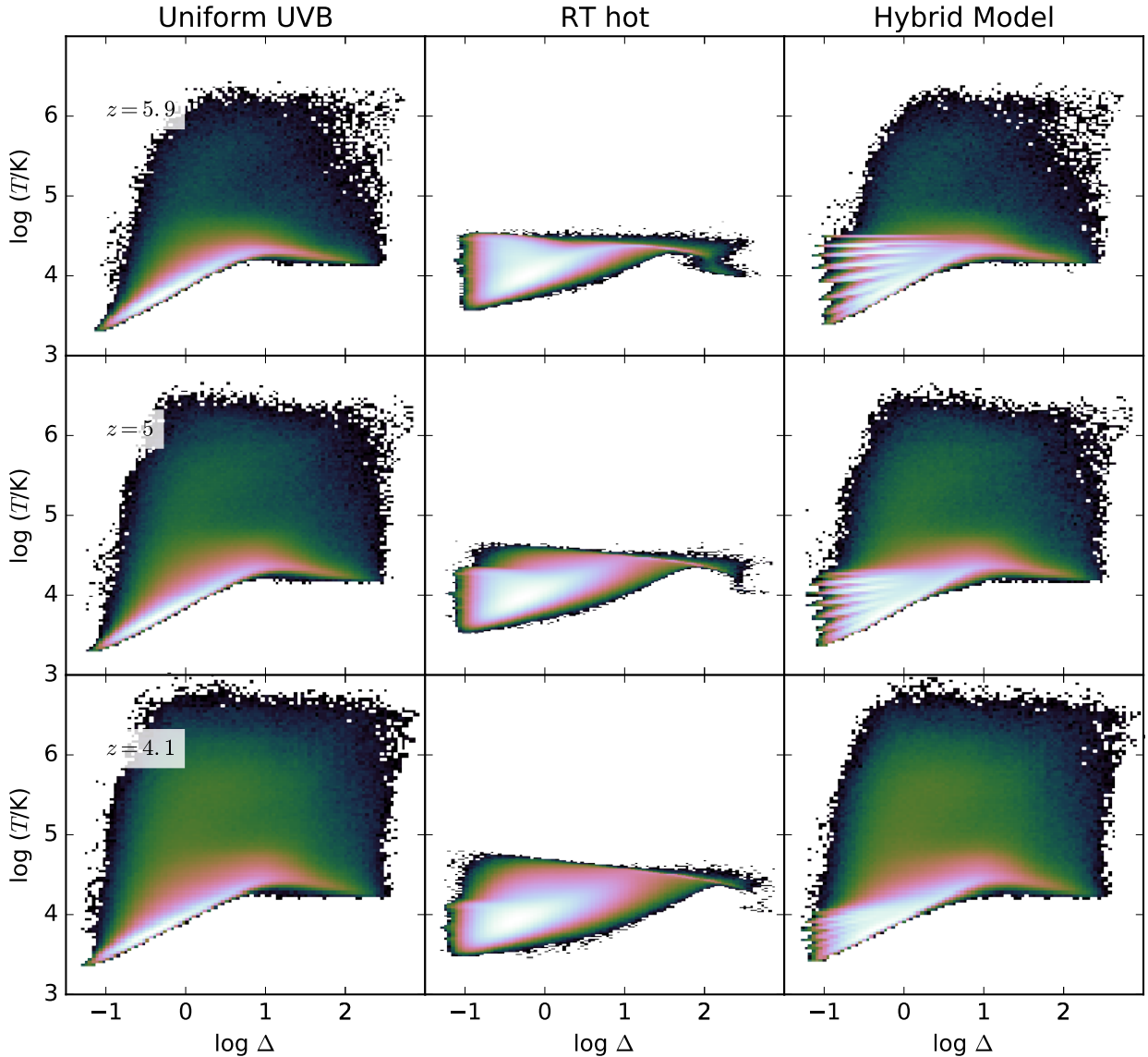


Figure 7. Volume-weighted temperature-density distribution of gas in the three models, at the same redshifts as in Figure 6. The radiative transfer and hybrid models both have more gas at $\log(T/K) \sim 4$ at $\log \Delta \lesssim 1$ than the uniform UVB model. No shock-heated gas ($\log(T/K) > 5$) is present in the radiative transfer run as the radiative transfer and the calculations of the thermal evolution are performed in post-processing.

These fluctuations persist down to $z \sim 4$ and occur on scales up to about 10 comoving Mpc, supporting the idea that they may affect statistical properties of Ly α forest data in the post-reionization IGM.

Figure 7 shows the volume-weighted temperature-density phase space occupied by the gas in our three models. The radiative transfer and hybrid models both contain hotter low-density gas than the uniform UVB run, due to the inhomogeneous reionization. The gas that reionized later will be hotter. This hot gas in the hybrid model looks like a discretised version of the same gas in the radiative transfer run, because of the finite number of optically thin simulations with different reionization redshifts we have run. Even at $z \sim 4$, there are still significant spatial fluctuations in the temperature-density relation $T(\Delta) = T_0 \Delta^{\gamma-1}$. There is no

clearly defined overall TDR as in the uniform UVB simulation. Indeed, in the radiative transfer run at $z \sim 6$ some of the low density gas has a temperature higher than gas at mean density. Attempting to fit a single relation to this distribution would result in a relation that flattens or inverts at low densities. This is in agreement with previous works studying the effect of hydrogen reionization on the TDR (Trac et al. 2008; Furlanetto & Oh 2009; Lidz & Malloy 2014). It is not clear whether the scatter in temperature should be detectable at $z \sim 4 - 5$. The largest scatter is found at low densities ($\log \Delta < -0.5$), but the “characteristic density” probed by the Ly α forest at those redshifts is just above the mean (Becker et al. 2011a). At lower redshifts, comparison with Ly α forest data is complicated by He II reionization (Rorai et al. 2017).

There are several differences worth noting between the three models. Firstly, shock-heated gas (with $T > 10^5$ K) is visible in both the hydrodynamic runs and is missing in the radiative transfer run which does not properly model heating due to hydrodynamic effects. This is because we estimate the heating/cooling rates due to changes in Δ from the snapshots in our hydrodynamic simulation, which are spaced 40 Myr apart. However, only a small fraction of the gas is this hot. Secondly, the temperature-density relation at densities $\Delta > 1$ in our radiative transfer run is broader than the hydrodynamic runs. This seems to be a result of doing the radiative transfer in post-processing. Since the temperature is not advected with the gas, a filament or halo moving across a cell can introduce some spurious heating. The turnover in the temperature-density relation occurs at a higher density than in the hydrodynamic runs. Finally, the highest density gas in the radiative transfer simulation is colder than in the hydrodynamic runs. This corresponds to the cells where self-shielding is important, and the neutral gas can cool more efficiently. Overall, the agreement between the radiative transfer simulations and the hybrid approach using a suite of optically thin simulations is remarkably good.

4 COMPARISON OF MOCK ABSORPTION SPECTRA WITH $\text{Ly}\alpha$ FOREST DATA

To understand the effect of these temperature inhomogeneities on observable quantities, we now test the models against statistics of the high-redshift $\text{Ly}\alpha$ forest: the distribution of effective optical depths, the flux power spectrum, the flux probability distribution function and the abundance of transmission spikes in the spectrum of ULAS J1120+0641. We construct synthetic $\text{Ly}\alpha$ absorption spectra along random sightlines through the volume, choosing the same sightlines for each of our models. These take into account peculiar velocities of the gas and the thermal broadening. The Voigt profiles are modelled as in [Tepper-García \(2006\)](#). In cases where we use a uniform UV background, we account for optically thick absorbers using the prescription outlined in [Rahmati et al. \(2013\)](#). For our hybrid model, we construct the spectra by taking sightlines through the grid we constructed from the instantaneous reionization models (as described in Section 2.3) and computing the optical depth using the properties of the cells along the sightline.

4.1 Effective Optical Depths

The effective optical depth is defined as $\tau_{\text{eff}} = -\log\langle F \rangle$, where $\langle F \rangle$ is the mean transmitted flux. To be consistent with [Becker et al. \(2015\)](#), we measure this quantity along spectra with comoving length 50 Mpc h^{-1} . This is longer than our 20 Mpc h^{-1} box, so we take 2.5 randomly selected spectra to represent one 50 Mpc h^{-1} segment. We rescale the optical depth of our synthetic spectra, so that the mean flux across our whole sample matches the mean flux where the observed distribution at $P(< \tau_{\text{eff}}) = 0.5$. This rescaling ranges from factors of 0.6-3.2, with the higher values typically occurring at lower redshifts. This is likely related to the high photoionization rate in our radiative transfer sim-

ulation (Figure 1). Our effective optical depth distributions are shown in Figure 8 in eight redshift bins.

As other works have found, it is not difficult to find models that agree with the observed optical depth distribution at $z \lesssim 5$ ([Becker et al. 2015](#); [Chardin et al. 2015](#)). Indeed, our models fit the data reasonably well and we see little difference between the uniform UVB model and the ones that try to model reionization more accurately. Around $z = 5.2 - 5.3$, however, we find that our radiative transfer and hybrid models begin to produce an increasingly wider distribution with increasing redshift than the uniform UVB model. It seems that this is due to the temperature fluctuations rather than any effect of the UV background. In [Chardin et al. \(2015\)](#), the radiative transfer simulations and the uniform UVB simulations produced nearly identical distributions in all redshift bins (after rescaling the mean flux). This is because, after overlap, there is very little fluctuation in the UV background. We similarly find a very sharply peaked distribution in our radiative transfer simulation. The temperature inhomogeneities, however, persist even after overlap has occurred, as discussed in Section 3. To test this further, we constructed a set of spectra taking the temperatures of the hybrid model and calculating the H I neutral fraction assuming the spatially uniform [Haardt & Madau \(2012\)](#) UV background. The distribution of effective optical depths measured from these spectra is broader than that for spectra where temperatures are taken from the uniform UVB simulation. This suggests that temperature rather than UV fluctuations are driving this scatter in τ_{eff} .

Our findings that temperature fluctuations due to patchy reionization result in a broader distribution of effective optical depths is qualitatively in agreement with the results presented by [D’Aloisio et al. \(2015\)](#). The distribution of optical depths we recover is, however, not as broad as in [D’Aloisio et al. \(2015\)](#). The difference may lie in exact details of the reionization history we assume, but we have chosen an extended reionization history finishing at $z \sim 6$ for our fiducial model. The difference may be due to the small volume we use in this work. Note, however, that we do not find any trends with box size, with our 20 and 40 Mpc h^{-1} boxes producing nearly identical results. However, these volumes are still much smaller than in [D’Aloisio et al. \(2015\)](#). The largest box we studied here has side length 40 Mpc h^{-1} vs. 400 Mpc h^{-1} used by [D’Aloisio et al. \(2015\)](#). Indeed, they argue that their distribution becomes broader as the spatial scale of the ionized regions increases and their best fit is for regions with length larger than our simulation box size. Another difference is that they assume that more massive haloes are responsible for reionization ($1.2 \times 10^8 M_{\odot}$ vs. $2 \times 10^9 M_{\odot}$). For a fixed total emissivity, using more massive haloes results in larger structures in the ionization field. This will result in variations of the temperature-density relation over larger spatial scales, and a correspondingly broader distribution of effective optical depths. The difference is unlikely to be due to our heating of the IGM due to the onset of He II reionization, as we see no difference between our radiative transfer runs (where this effect is missing) and the hybrid model (where it is included). In [D’Aloisio et al. \(2015\)](#), the authors argue that they do not recover the largest observed optical depths in the highest redshift bins due to their semi-numerical method. This method combines a reionization his-

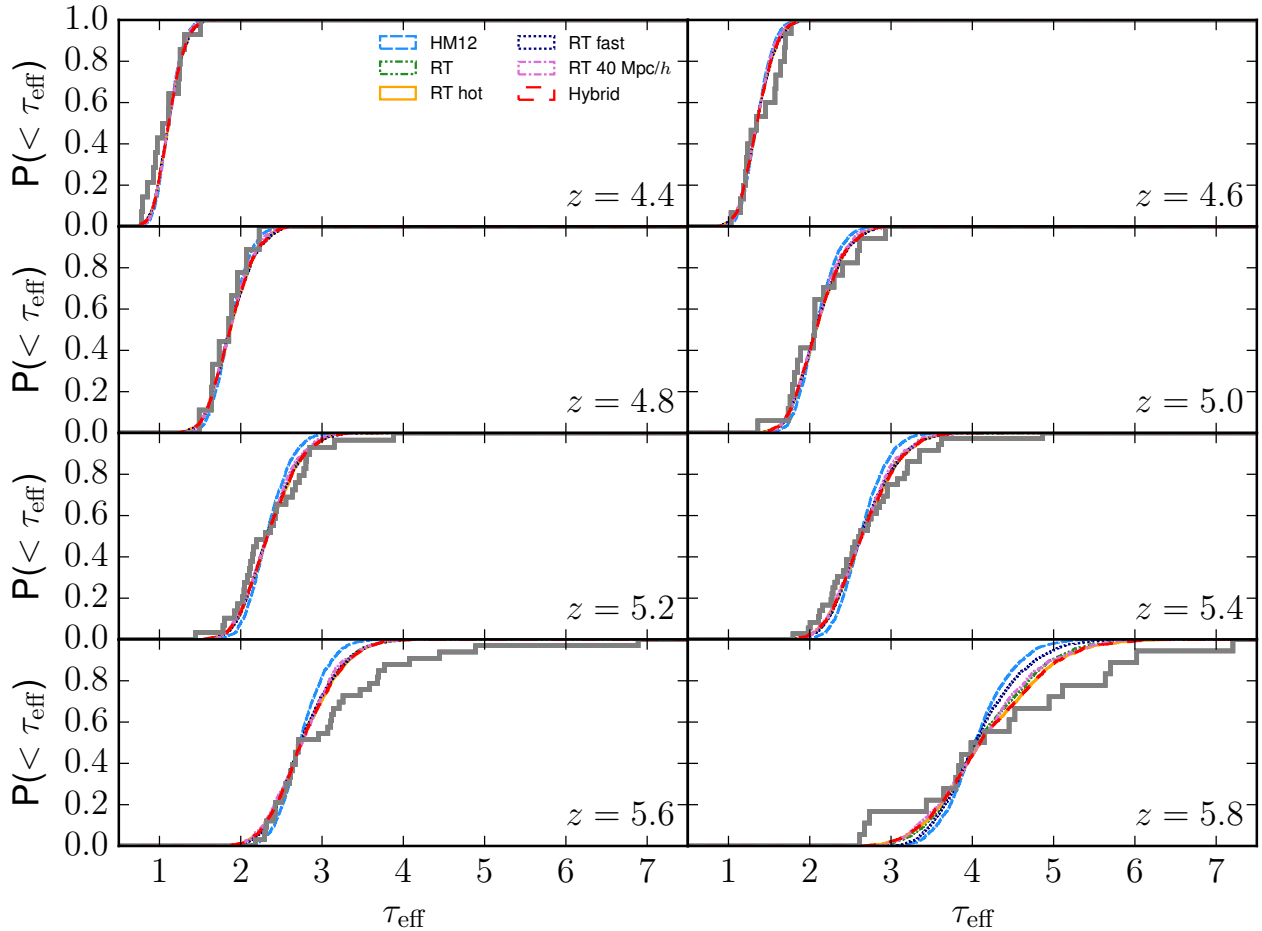


Figure 8. Cumulative distribution of effective optical depths measured in $50 \text{ Mpc } h^{-1}$ chunks for the three models in eight redshift bins. The coloured lines are distributions from our different models. Plotted in grey thick lines are the observations from [Becker et al. \(2015\)](#) and [Fan et al. \(2006\)](#).

tory from their large $400 \text{ Mpc } h^{-1}$ volume with sightlines taken from higher resolution $12.5 \text{ Mpc } h^{-1}$ boxes, the result of which is that the reionization redshift does not correlate with density along their sightlines. In our case, this is not an issue, but nevertheless we also do not recover these large effective optical depths due to the temperature fluctuations alone. [Davies et al. \(2017\)](#) have also used a semi-numerical method to model temperature fluctuations that do correlate with the density field in a $546 \text{ Mpc } h^{-1}$ box. In their case, they are able to recover the largest effective optical depths, but note that, as discussed before, they assume higher temperatures due to reionization than in our preferred models (see also [Puchwein et al. 2018](#)).

Looking at the other radiative transfer runs, we find that the optical depth PDF is slightly narrower for the runs with $E_\gamma = 18.4 \text{ eV}$. Note again that this lower photon energy was required to match the measurements of the IGM temperature (Section 3). For a model that matches both the Ly α forest temperature constraints and has a reionization history consistent with the [Planck Collaboration XLVII \(2016\)](#) measurement of the optical depth to reionization (the RT fast run), we find only a small difference from the uniform UVB model. We find no difference between the different inhomogeneous temperature models for the bins with $z \leq 5.6$.

As we have discussed earlier accurate modelling of all the relevant effects is still very challenging and will ultimately require very high-dynamic range multi-frequency radiative transfer simulations, but our simulation appear to already suggest that for models consistent with the temperature evolution of the IGM the spatial fluctuations of the TDR are probably about a factor two or more too small to explain the large observed opacity fluctuations on large ($\geq 50 \text{ } h^{-1}$ comoving Mpc) scales at $z \gtrsim 5$.

4.2 Flux Power Spectra and Probability Distribution of Transmitted Flux

We next investigate the effect of our different models on the high-redshift flux power spectrum. Again, at each redshift our flux is rescaled; this time to match the mean flux of the observations quoted in [Viel et al. \(2013\)](#). We compute the power spectrum of the fractional transmission $\delta_F = F/\langle F \rangle - 1$, where F is the flux and $\langle F \rangle = e^{-\tau_{\text{eff}}}$ is the mean flux of all sightlines at that redshift. We show the resulting power spectra in Figure 9 in four different redshift bins. Plotted for comparison are results for the flux power spectra from

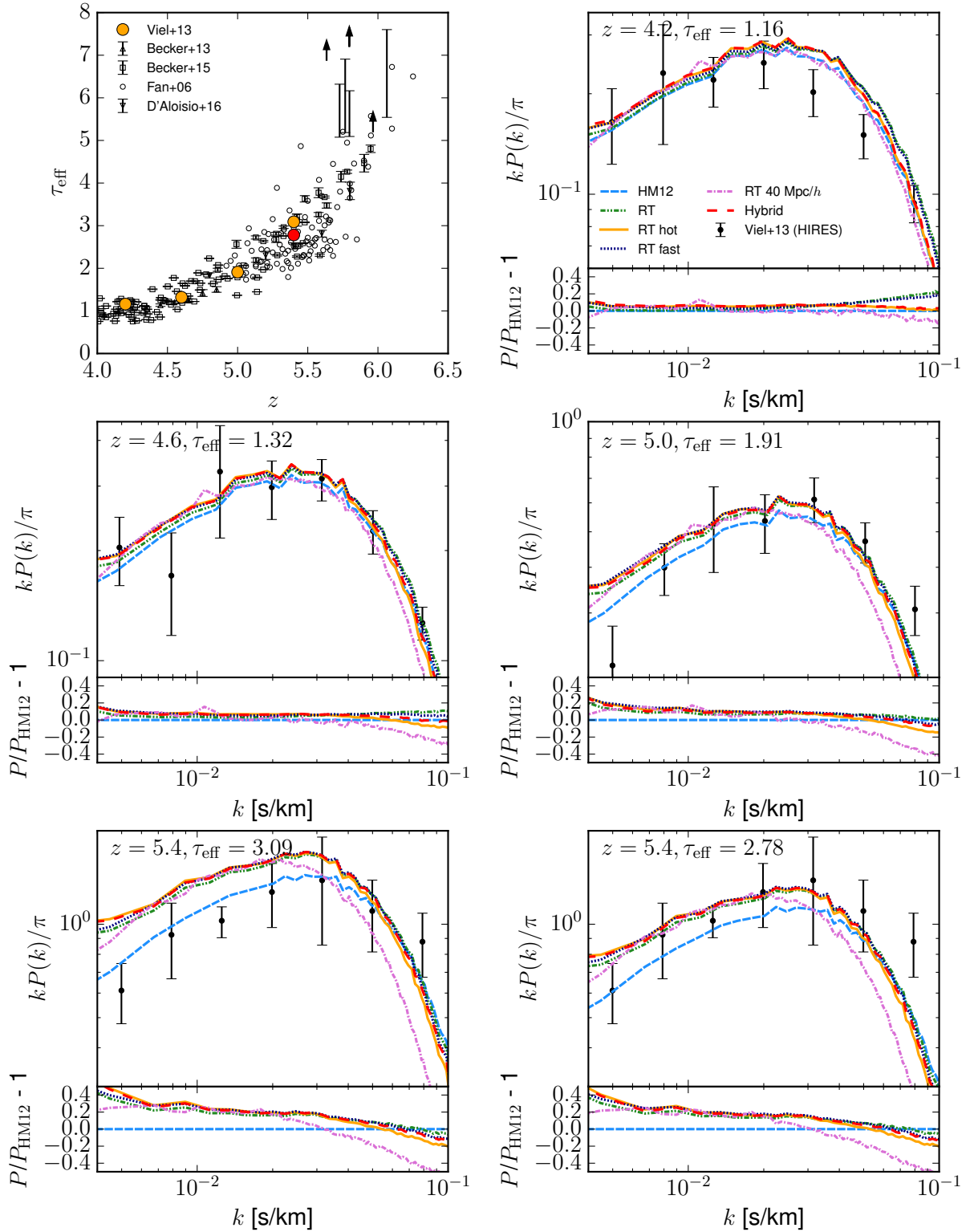


Figure 9. Shown in the top left is the evolution of the effective optical depth with redshift. Shown in black are data from [Fan et al. \(2006\)](#), [Becker & Bolton \(2013\)](#) and [Becker et al. \(2015\)](#). The orange circles are the best fit effective optical depths from [Viel et al. \(2013\)](#), to which we scale our spectra here. The red circle shows the effective optical depth at $z = 5.4$ decreased by 10 per cent, to which we scale our spectra in the bottom right panel. This value is still within the 1σ confidence limits quoted in [Viel et al. \(2013\)](#). The other panels show the flux power spectra for the different models in four redshift bins. The bin at $z = 5.4$ is shown twice for models rescaled to different effective optical depths. The coloured lines are distributions from our different models. Plotted in black are the observations from [Viel et al. \(2013\)](#). Below each panel, the power spectra relative to the uniform UVB simulation are shown.

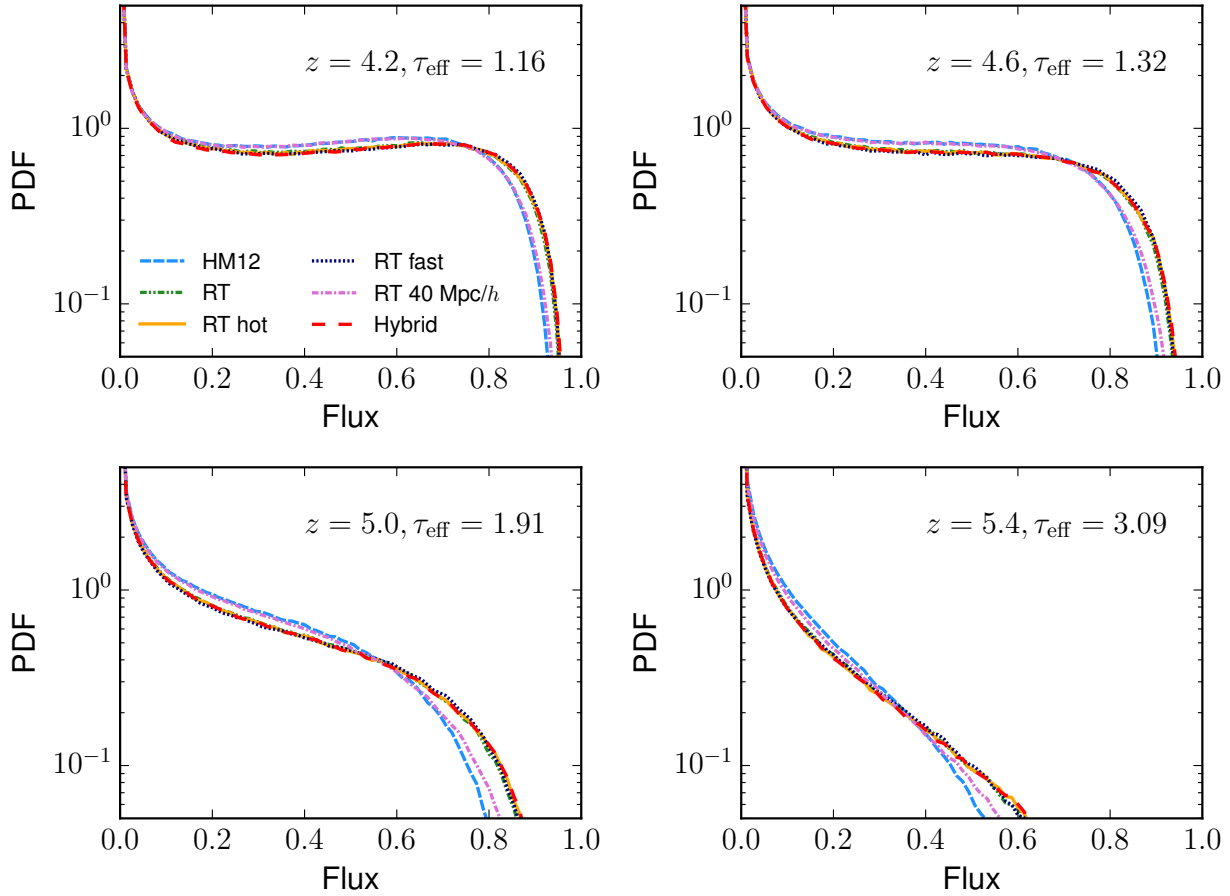


Figure 10. Flux PDF in our different models in four different redshift bins, after they have been rescaled to the same mean flux and sampled onto 10 km s^{-1} pixels. For simulations with the same resolution, the models with a spatially varying TDR predict more high-flux pixels.

Viel et al. (2013). These power spectra are constructed from high-resolution spectra of quasars presented in Becker et al. (2007, 2011a,b) and Calverley et al. (2011). Note that we do not include a continuum correction as in Bolton et al. (2017). At $z = 4.2$ and 4.6 there is little difference between the models, similar to what we found for the effective optical depth distributions in Section 4.1.

We find, however, a difference at small scales in the power spectra calculated using our 20 and $40 \text{ Mpc } h^{-1}$ boxes, suggesting that our results are not converged at this resolution (see also Oñorbe et al. 2017). This may explain why our models are not matching the observations at the smallest scales. It is still instructive to look at the differences between the models, however. As we are doing the radiative transfer in post-processing, we are not taking into account the effect of the different pressure smoothing for different thermal histories. Any differences at large k in the radiative transfer runs are therefore due to thermal broadening alone. Reassuringly, we find little difference between the RT hot run and the hybrid model (which, as it is constructed from a grid of hydrodynamic models, does account for the effect of pressure smoothing).

In the highest redshift bin, at $z = 5.4$, excess power (10-20 per cent) at large scales ($k \lesssim 7 h \text{ Mpc}^{-1} = 5 \times 10^{-2}$

$\text{km}^{-1} \text{ s}$) becomes evident for the radiative transfer simulations if the optical depth in the simulated spectra matched that advocated by Viel et al. (2013). The difference reaches about a factor of 2 increase in power at the largest scales. This is in contrast with the result of D’Aloisio et al. (2018) who find that their temperature fluctuation model shows increased power at scales $k \lesssim 0.2 h \text{ Mpc}^{-1}$ ($k \lesssim 1.5 \times 10^{-3} \text{ km}^{-1} \text{ s}$). This is likely due to the difference in the spatial scale of our temperature fluctuations. As we have already mentioned, the fluctuations in the simulations of D’Aloisio et al. (2018) occur mainly on scales larger than the box-size of our simulations. Our results are in better agreement with that of Cen et al. (2009) (who simulated a $100 h^{-1} \text{ Mpc}$ volume), both in the scales at which this increased power becomes important and the amplitude of the increase.

At $z = 5.4$, the models with a spatially varying TDR seem to be a poorer match to the observations than the uniform UVB model. This is somewhat surprising, as in section 4.1, we found that including the inhomogeneities improved the agreement between observations and simulations at $z = 5.8$. This may suggest that the temperature inhomogeneities could play a role, but in our simulations they do not extend to sufficiently large scales due to the limitations of the rather small box size of our simulations. It could also

suggest that spatial fluctuations of the TDR improving the agreement of the PDF of the opacity at $z = 5.8$ are already much less important by $z = 5.4$ (note that the uniform UVB simulation provided a reasonably good match to the effective optical depth PDF at that redshift). As shown in the upper left panel of Figure 9 and as discussed before, at $z \gtrsim 5.4$ the fluctuations in the effective optical depth have begun to rise significantly. In the bottom right panel we therefore show the flux power spectrum for this redshift with a somewhat smaller effective optical depth as indicated by the red circle in the upper left panel. This improves the agreement at large scales, but increases the discrepancy between the models and data at small scales. Note again, however, that our simulations are not fully converged at small scales.

Next we look at the probability density distribution of the transmitted flux (Figure 10). Again, all the spectra are rescaled to the same mean flux. Compared with the uniform UVB simulation, the radiative transfer runs at the same resolution predict more pixels with high flux and more pixels with no flux at all. This is similar to what was found by Gallerani et al. (2006) when comparing models with early and late reionization histories. Another way of showing this difference would be to look at the distribution of dark gaps and peak heights in the spectra, as presented in Gnedin et al. (2017).

Spatial variations in the TDR of the IGM have been identified as a source of uncertainty in Ly α forest constraints on warm dark matter (WDM) models (e.g. Hui et al. 2017). We do find that the models including temperature fluctuations due to reionization do suppress power on small scales ($k > 0.05 - 0.06 \text{ km}^{-1} \text{ s}$), but this seems to be a smaller effect than in Viel et al. (2013) where the suppression begins at $k \sim 0.01 \text{ km}^{-1} \text{ s}$ in their WDM models compared to the best-fit CDM model. For the RT fast run this suppression of power results in a difference of about 10 per cent at the smallest scale observed. Hui et al. (2017) argue that modelling the temperature fluctuations should increase power on small scales. We do not see that here, rather seeing a suppression of power in our radiative transfer runs due to the thermal broadening of the lines. We reiterate however that our simulations are not converged at the smallest scales. Higher resolution simulations, ideally also accounting for the pressure smoothing of the gas due to photoheating, would be required to further investigate this.

4.3 Transmission Spikes and Trough Length in the spectrum of ULAS J1120+0641

Analysis of a VLT/X-shooter spectrum of the $z = 7.1$ quasar ULAS J1120+0641 by Barnett et al. (2017) showed seven transmission spikes in the Ly α forest in the range $5.86 < z < 6.12$, followed by a Gunn-Peterson trough of length $240 h^{-1} \text{ cMpc}$. Chardin et al. (2018) recently showed that these features can be reproduced in radiative transfer simulations calibrated to match Ly α forest data after reionization, provided they assume an enhanced temperature in the voids of $T = 10^4 \text{ K}$. As we already take these large-scale temperature fluctuations into account, we also investigate the occurrence of transmission spikes and troughs in our simulations. The observed trough extends over scales much larger than our $20 \text{ Mpc } h^{-1}$ simulations. However, we note that the nature of this trough is different to the deepest

troughs at $z \sim 6$ in that no Ly β flux is observed at the same redshifts. It is therefore reasonable to speculate that this trough is due to an increasingly neutral IGM, in which case our boxsize should not be a limitation.

Following Chardin et al. (2018), we construct spectra by taking sightlines through six different simulation outputs. We stitch randomly selected sightlines together to produce a spectrum that covers the redshift range $5.86 < z < 7.04$. We multiplied the spectrum with a power-law $f_\lambda \propto \lambda^{-0.5}$ (to account for the intrinsic shape of the quasar spectrum). We sampled the spectrum onto 10 km s^{-1} pixels, convolved the spectrum with a instrument profile suitable for X-shooter and added noise appropriate to this observation. We note that our results are insensitive to changing the standard deviation of the noise by a factor of 2. We searched for spikes using a Gaussian matched filter with standard deviation 15 km s^{-1} and identified the regions in our spectra that had a signal-to-noise ratio greater than 5.

In Figure 11, we show the transmission spikes, trough lengths and total transmitted flux measured from these spectra. The trough length is defined as the distance between the redshift of the last spike and $z = 7.04$. We find that for models that have the same photoionization rate at $z \sim 6$ (the RT and RT hot runs), the different temperatures in these simulations increases the number of spikes by almost a factor of two. For the models that have the same excess photon energy but different reionization histories (the RT and RT fast runs), we again find very different distributions of spikes. This is likely driven by the difference in photoionization rate, as the temperature at $z = 6$ is not very different in the two runs (see Figure 5). For the number of spikes, the length of the trough and the total integrated flux, the observations presented in Barnett et al. (2017) seems to sit between the RT and RT fast runs. This may suggest that a model with this temperature is favoured, but that a photoionization rate that sits somewhere between the two models is required. This would be in the range $1 - 3 \times 10^{-13} \text{ s}^{-1}$ at $z = 6$. However, this conclusion is highly sensitive to the reionization history assumed.

To make a connection with Chardin et al. (2018), who do not model temperature fluctuations due to reionization, we also looked into the impact of changing the temperatures in the voids on these statistics by combining the photoionization rates from our radiative transfer models with the temperatures taken from our optically thin simulation. Once we assume that the voids are at a lower temperature (a few times $T = 10^3 \text{ K}$), the number of spikes detected drops significantly as the gas temperature drops (see also Chardin et al. 2018). For example, with a photoionization rate taken from the RT model, the median number of spikes detected changes from 20 to 8 once the temperatures from the optically thin run are used.

5 SUMMARY AND CONCLUSIONS

We have presented here radiative transfer simulations of the thermal history of the IGM during and directly after the epoch of hydrogen reionization and compared them to simulations with a uniform ionizing UV background as well as a hybrid approach based on a suite of optically thin simulations for a range of reionization redshifts. Our radiative

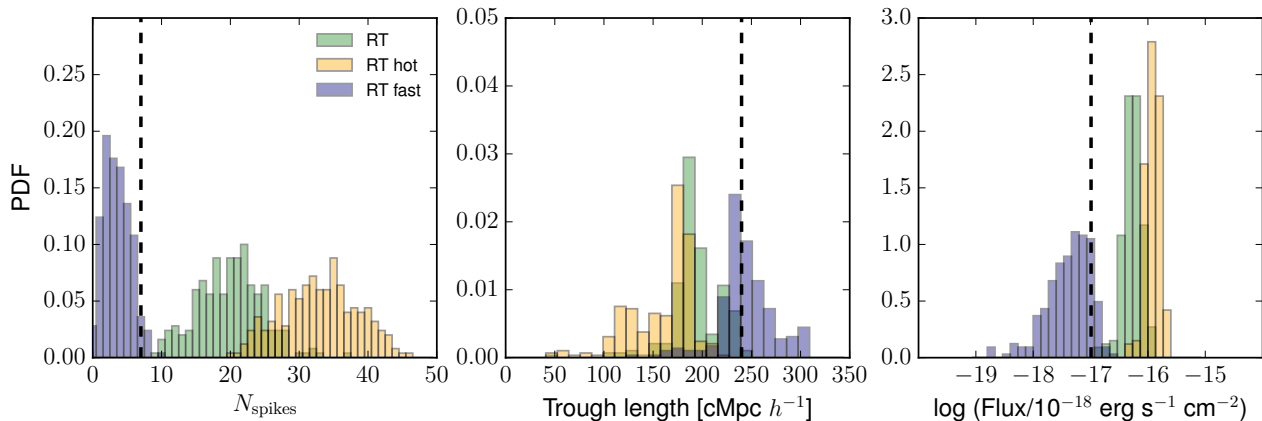


Figure 11. The probability density functions of the number of spikes (left), trough lengths (middle) and total flux integrated over the detected spikes (right) measured in the RT (green), RT hot (orange) and RT fast (blue) simulations. In each panel, the black dashed line represents the measurements of each quantity taken from Barnett et al. (2017).

transfer simulations were calibrated to match Ly α forest constraints on properties of the lower redshift IGM, such as the neutral fraction and photoionization rate. We explored the effects of using different energies of ionizing photons, different boxsizes and different reionization histories. We then compared these simulations to the distribution of effective optical depths and the flux power spectrum at $z > 4$.

For simulations where the gas receives a temperature boost at reionization similar to that used in D’Aloisio et al. (2015), we find that we still cannot match the PDF of effective optical depths in the highest redshift bins. We note however that these simulations have been performed in volumes far smaller than the semi-numerical studies by D’Aloisio et al. (2015) and Davies et al. (2017), who both find that temperature fluctuations can explain the fluctuations in the opacity of the Ly α forest. This could be explained by effects not captured here, such as large-scale clustering of galaxies. Using a photon energy high enough to reach such a high temperature boost also puts the simulations in tension with measurements of the temperature of the IGM at $z \lesssim 5$, and with the number of transmission spikes detected above $z = 5.86$ in the spectrum of ULAS J1120+0641 (although this will be sensitive to the assumed reionization history). For radiative transfer simulations that match Ly α forest constraints on the photoionization rate and the temperature at mean density, we find that the simulations predict a significantly smaller broadening of the effective optical depth PDF. If we choose our reionization history to also fall close to the Planck Collaboration XLVII (2016) constraint on the optical depth to reionization, we clearly fail to match the PDF in the highest redshift bin. The spatial fluctuations of the TDR of the IGM in these models appear to be about a factor two too small to explain the large observed opacity fluctuation on large ($\geq 50 h^{-1}$ comoving Mpc) scales at $z \gtrsim 5.5$. Higher dynamic range and multi-frequency radiative transfer simulations will be required to answer this question more accurately. We find little difference between the results obtained from the “hybrid” model and the radiative transfer simulations performed in post-processing. This suggests that the hydrodynamic response of the gas does not have a large effect on the Ly α statistics we have considered.

Our radiative transfer simulations with spatial fluctuations of the TDR of the IGM require a lower effective optical depth to match the observed flux power spectra at the highest redshift, compared to the standard modelling with a uniform UV background. The position of the cut-off in the power spectrum is affected very little in the radiative transfer simulations. This suggests that the effect of spatial fluctuations of the TDR of the IGM on constraints on the free-streaming of dark matter is rather small. To make more quantitative statements, radiative transfer simulations of WDM models will be required.

ACKNOWLEDGEMENTS

We would like to thank Jonathan Chardin for helpful discussions. We would like to thank Volker Springel for making P-GADGET3 available. We would also like to thank both Andreas Bauer and Volker Springel for making their radiative transfer code available. LCK acknowledges the support of a CITA postdoctoral fellowship, an Isaac Newton studentship, the Cambridge Trust and STFC. Support by the FP7 ERC Advanced Grant Emergence-320596 is gratefully acknowledged. EP acknowledges support from the Kavli Foundation. This work used the DiRAC Data Analytic system at the University of Cambridge, operated by the University of Cambridge High Performance Computing Service on behalf of the STFC DiRAC HPC Facility (www.dirac.ac.uk). This equipment was funded by BIS National E-infrastructure capital grant (ST/K001590/1), STFC capital grants ST/H008861/1 and ST/H00887X/1, and STFC DiRAC Operations grant ST/K00333X/1. DiRAC is part of the National E-Infrastructure. This research was supported by the Munich Institute for Astro- and Particle Physics (MIAPP) of the DFG cluster of excellence “Origin and Structure of the Universe”.

REFERENCES

Abel T., Haehnelt M. G., 1999, *ApJ*, **520**, L13

- Barnett R., Warren S. J., Becker G. D., Mortlock D. J., Hewett P. C., McMahon R. G., Simpson C., Venemans B. P., 2017, *A&A*, **601**, A16
- Bauer A., Springel V., Vogelsberger M., Genel S., Torrey P., Sijacki D., Nelson D., Hernquist L., 2015, *MNRAS*, **453**, 3593
- Becker G. D., Bolton J. S., 2013, *MNRAS*, **436**, 1023
- Becker R. H., et al., 2001, *AJ*, **122**, 2850
- Becker G. D., Rauch M., Sargent W. L. W., 2007, *ApJ*, **662**, 72
- Becker G. D., Bolton J. S., Haehnelt M. G., Sargent W. L. W., 2011a, *MNRAS*, **410**, 1096
- Becker G. D., Sargent W. L. W., Rauch M., Calverley A. P., 2011b, *ApJ*, **735**, 93
- Becker G. D., Bolton J. S., Madau P., Pettini M., Ryan-Weber E. V., Venemans B. P., 2015, *MNRAS*, **447**, 3402
- Bolton J. S., Becker G. D., 2009, *MNRAS*, **398**, L26
- Bolton J. S., Haehnelt M. G., 2007a, *MNRAS*, **374**, 493
- Bolton J. S., Haehnelt M. G., 2007b, *MNRAS*, **382**, 325
- Bolton J. S., Becker G. D., Raskutti S., Wyithe J. S. B., Haehnelt M. G., Sargent W. L. W., 2012, *MNRAS*, **419**, 2880
- Bolton J. S., Puchwein E., Sijacki D., Haehnelt M. G., Kim T.-S., Meiksin A., Regan J. A., Viel M., 2017, *MNRAS*, **464**, 897
- Calverley A. P., Becker G. D., Haehnelt M. G., Bolton J. S., 2011, *MNRAS*, **412**, 2543
- Cen R., 1992, *ApJS*, **78**, 341
- Cen R., McDonald P., Trac H., Loeb A., 2009, *ApJ*, **706**, L164
- Chardin J., Haehnelt M. G., Aubert D., Puchwein E., 2015, *MNRAS*, **453**, 2943
- Chardin J., Puchwein E., Haehnelt M. G., 2017, *MNRAS*, **465**, 3429
- Chardin J., Haehnelt M. G., Bosman S. E. I., Puchwein E., 2018, *MNRAS*, **473**, 765
- Choudhury T. R., Haehnelt M. G., Regan J., 2009, *MNRAS*, **394**, 960
- D'Aloisio A., McQuinn M., Trac H., 2015, *ApJ*, **813**, L38
- D'Aloisio A., McQuinn M., Davies F. B., Furlanetto S. R., 2018, *MNRAS*, **473**, 560
- Davies F. B., Furlanetto S. R., 2016, *MNRAS*, **460**, 1328
- Davies F. B., Becker G. D., Furlanetto S. R., 2017, preprint, ([arXiv:1708.08927](https://arxiv.org/abs/1708.08927))
- Fan X., et al., 2006, *AJ*, **132**, 117
- Furlanetto S. R., Oh S. P., 2005, *MNRAS*, **363**, 1031
- Furlanetto S. R., Oh S. P., 2009, *ApJ*, **701**, 94
- Furlanetto S. R., Zaldarriaga M., Hernquist L., 2004, *ApJ*, **613**, 16
- Gallerani S., Choudhury T. R., Ferrara A., 2006, *MNRAS*, **370**, 1401
- Gnedin N. Y., 2000, *ApJ*, **542**, 535
- Gnedin N. Y., Becker G. D., Fan X., 2017, *ApJ*, **841**, 26
- Haardt F., Madau P., 2012, *ApJ*, **746**, 125
- Hui L., Gnedin N. Y., 1997, *MNRAS*, **292**, 27
- Hui L., Ostriker J. P., Tremaine S., Witten E., 2017, *Phys. Rev. D*, **95**, 043541
- Iliev I. T., Mellema G., Pen U.-L., Merz H., Shapiro P. R., Alvarez M. A., 2006, *MNRAS*, **369**, 1625
- Iliev I. T., Mellema G., Ahn K., Shapiro P. R., Mao Y., Pen U.-L., 2014, *MNRAS*, **439**, 725
- Iršič V., et al., 2017, *Phys. Rev. D*, **96**, 023522
- Keating L. C., Haehnelt M. G., Cantalupo S., Puchwein E., 2015, *MNRAS*, **454**, 681
- Lidz A., Malloy M., 2014, *ApJ*, **788**, 175
- Madau P., Haardt F., Rees M. J., 1999, *ApJ*, **514**, 648
- Miralda-Escudé J., Rees M. J., 1994, *MNRAS*, **266**, 343
- Miralda-Escudé J., Haehnelt M., Rees M. J., 2000, *ApJ*, **530**, 1
- Oñorbe J., Hennawi J. F., Lukić Z., 2017, *ApJ*, **837**, 106
- Osterbrock D. E., Ferland G. J., 2006, *Astrophysics of gaseous nebulae and active galactic nuclei*. University Science Books
- Pawlik A. H., Schaye J., 2011, *MNRAS*, **412**, 1943
- Peebles P. J. E., 1971, *Physical cosmology*. Princeton University Press
- Planck Collaboration XIII 2016, *A&A*, **594**, A13
- Planck Collaboration XLVII 2016, *A&A*, **596**, A108
- Prochaska J. X., Worseck G., O'Meara J. M., 2009, *ApJ*, **705**, L113
- Puchwein E., Bolton J. S., Haehnelt M. G., Madau P., Becker G. D., Haardt F., 2015, *MNRAS*, **450**, 4081
- Puchwein E., Haardt F., Haehnelt M. G., Madau P., 2018, preprint, ([arXiv:1801.04931](https://arxiv.org/abs/1801.04931))
- Rahmati A., Pawlik A. H., Raičević M., Schaye J., 2013, *MNRAS*, **430**, 2427
- Rorai A., et al., 2017, *MNRAS*, **466**, 2690
- Songaila A., 2004, *AJ*, **127**, 2598
- Springel V., 2005, *MNRAS*, **364**, 1105
- Tepper-García T., 2006, *MNRAS*, **369**, 2025
- Trac H., Cen R., Loeb A., 2008, *ApJ*, **689**, L81
- Upton Sanderbeck P. R., D'Aloisio A., McQuinn M. J., 2016, *MNRAS*, **460**, 1885
- Viel M., Haehnelt M. G., Springel V., 2004, *MNRAS*, **354**, 684
- Viel M., Lesgourgues J., Haehnelt M. G., Matarrese S., Riotto A., 2005, *Phys. Rev. D*, **71**, 063534
- Viel M., Becker G. D., Bolton J. S., Haehnelt M. G., 2013, *Phys. Rev. D*, **88**, 043502
- White R. L., Becker R. H., Fan X., Strauss M. A., 2003, *AJ*, **126**, 1
- Worseck G., et al., 2014, *MNRAS*, **445**, 1745
- Wyithe J. S. B., Bolton J. S., 2011, *MNRAS*, **412**, 1926

This paper has been typeset from a \LaTeX file prepared by the author.